Space-local spectral texture segmentation applied to characterizing the heterogeneity of hydraulic conductivity

Greg A. Oldenborger,[1] Robert A. Schincariol, and Lalu Mansinha

Department of Earth Sciences, University of Western Ontario, London, Ontario, Canada

Received 5 March 2001; revised 6 March 2002; accepted 12 March 2002; published 24 August 2002.

[1] Spatial variability of hydraulic conductivity exerts a predominant control on groundwater flow by influencing advective pathways, hydrodynamic dispersion, and density-dependent instabilities. Space-local spectral texture segmentation aids in the macroscale characterization of the spatial heterogeneity of natural porous media via an outcrop analogue approach. Detailed photographic data sets were obtained for a 45 m $\times$ 3 m vertical section of glacial-fluvial sand and gravel deposit in the Fanshawe Delta area (Ontario, Canada). High-resolution texture maps of the sedimentary exposure are generated using a texture segmentation routine based on the space-local S transform with the photographic data sets used as input. Geostatistical analyses of the texture maps reveal similarity between the spatial correlation structures of spectral texture and hydraulic conductivity as determined from constant-head permeameter testing of sediment cores. Conditioned on the permeameter measurements, texture maps can be used to provide local continuous estimates of the hydraulic conductivity field at a spatial resolution equal to the sediment core dimensions. *INDEX TERMS:* 1829 Hydrology: Groundwater hydrology; 1894 Hydrology: Instruments and techniques; *KEYWORDS:* texture segmentation, hydraulic conductivity, heterogeneity, S transform

1. Introduction

[2] Spatial variability of hydraulic conductivity or intrinsic permeability exerts a predominant control on groundwater flow. Single order-of-magnitude contrasts in hydraulic conductivity may subtly influence the fluid potential and greatly influence the flow field, producing preferential paths for advective transport [*Gillham and Cherry*, 1982; *Yeh et al.*, 1995]. Heterogeneity of the porous media controls the macrodispersive component of the mechanical dispersion of solutes due to local-scale variations in groundwater velocity [*Gelhar and Axness*, 1983; *Frind et al.*, 1987]. In the case of variable density flow, heterogeneities are a controlling factor in the generation of plume instabilities [*Schincariol et al.*, 1997]. Accordingly, the character of the spatial distribution of hydraulic conductivity is a key input parameter for studies of contaminant transport, risk management for waste disposal, petroleum reservoir engineering, and general groundwater flow modeling.

[3] Large-scale descriptions of lithofacies and hydrofacies have proven inadequate for accurate predictions of groundwater flow and contaminant transport and dispersion [*Sudicky et al.*, 1983; *Anderson*, 1989; *Poeter and Gaylord*, 1990]. *Koltermann and Gorelick* [1996] reviewed several techniques being developed to address the need for representations of hydraulic property fields with increased spatial resolution. Generally, these representations of hydraulic property fields may take deterministic or stochastic forms. In the case of deterministic techniques, a single estimation of the hydraulic property field is developed through a combination of intense direct sampling and/or sophisticated interpolation and extrapolation techniques. Stochastic techniques, however, employ the spatial statistics of the hydraulic property (typically estimated via direct sampling) to generate any number of equally probable hydraulic property fields, all of which honor the observed spatial statistics. These multiple field generations are often used to investigate fluid flow problems in a Monte Carlo fashion. Minimum requirements for both deterministic and stochastic field estimation are a priori knowledge of the probability distribution of the hydraulic property and its spatial correlation structure. To this end, much focus of recent research has shifted toward attempts to incorporate remote sensing and data fusion into hydraulic property estimation in a groundwater context [e.g., *Hyndman and Gorelick*, 1996; *Cassiani and Medina*, 1997; *Hubbard et al.*, 1999].

[4] This paper investigates the applicability of a space-local spectral texture segmentation routine for characterizing the spatial distribution of hydraulic conductivity via an outcrop analogue approach. Texture may be defined as the combination of the magnitude and frequency of tonal change in an image; tone refers to the magnitude of the image variable and combinations of similar textures result in patterns [*Drury*, 1993]. Image may be generalized to refer to any two-dimensional representation of a scalar variable such as elevation, temperature or traditional photographic intensity. If the variable responsible for tonal change is grain size or grain size distribution, then sedimentary materials may be physically characterized or segmented (into patterns) by image texture. Furthermore, local empirical relationships between grain size distribution and hydraulic conductivity are well documented and often take the form of the Kozeny-Carman equation [*Mavko et al.*, 1998]. Thus the ability to

[1] Now at Center for Geophysical Investigation of the Shallow Subsurface, Boise State University, Boise, Idaho, USA.

0043-1397/02/2001WR000496$09.00

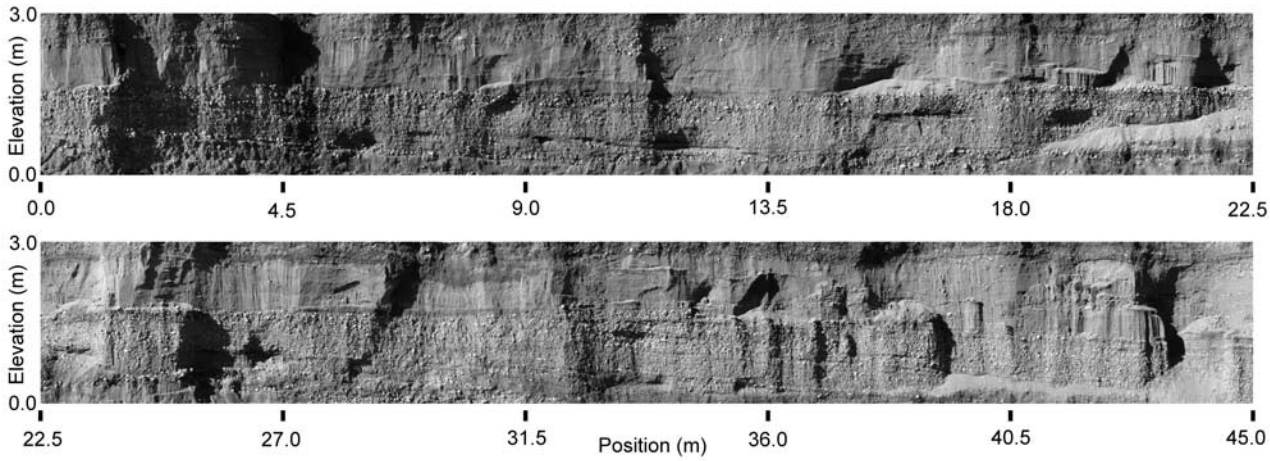

Figure 1. Photographic mosaic of the subsection data set for the Fanshawe section. Pixel resolution is 1.7 mm.

continuously map aquifer texture should provide estimates of aquifer heterogeneity and may provide a proxy for the spatial distribution of hydraulic conductivity.

[5] *Jussel et al.* [1994] attempted a manual texture segmentation of an aquifer in Switzerland using photographic images. Pattern delineation, however, was limited to the meter-scale due to the inherent limitations of clear geotechnical classification. The need for a more continuous, unbiased, and reproducible texture segmentation technique led *Eramian et al.* [1999] to the development of an automated texture segmentation algorithm. Many techniques exist for automated texture segmentation of images based on edge detection, pattern recognition (neural networks), or local image-domain properties; *Pal and Pal* [1993] provide a review. Often, automated segmentation works well only for images with sharp boundaries or a few distinct textures. To address these problems, *Eramian et al.* [1999] employed an innovative space-local frequency transform: the S transform. Using photographic images of a glacio-fluvial sand and gravel outcrop, encouraging correlation was reported between textures determined from S transform analysis and representative grain diameters determined from sieve analysis of sediment samples. The following investigation builds on these results by improving spatial accuracy and by developing an alternative texture segmentation algorithm. Furthermore, correlation is extended from a grain size versus texture relationship to a hydraulic conductivity versus texture relationship and the geostatistical characteristics of texture are calculated for the Fanshawe section.

1.1. Study Area

[6] The study area (the Fanshawe section) is located in an active gravel pit near London, Ontario, Canada at the latitude and longitude of 43.0634°N, 81.2088°E. The site was chosen for the vertical cliff exposure present due to the active mining of construction materials, for the ease of access, and for its sedimentary nature as a glacial-fluvial outwash deposit [*Barnett et al.*, 1991]. The Fanshawe Delta is predominantly composed of glacial-fluvial sands and gravels, coarsening from sand and silt in the southwest to alternating beds of sand and gravel in the northeast [*Dreimanis et al.*, 1998]. The geological setting combined with observed moderate heterogeneity makes the site applicable as an analogue to other aquifer sediments such as the Cape Cod aquifer [*Hess et al.*, 1992].

[7] The Fanshawe section (Figure 1) is an approximately North-South striking, vertical exposure of the northern Fanshawe Delta with a horizontal dimension of 45 m and a vertical dimension of 3 m. The deposit consists of horizontally bedded, internally sorted sand and gravel with occasional layers of sandy silt. Some flow features are visible in the section, such as scour depressions and cross beds. Gravel diameters for the Fanshawe section are typically below 50 mm with the lithology dominated by limestone and dolostone [*Dreimanis et al.*, 1998]. Cementation, however, is minor and the section is very susceptible to erosion by wind, water and gravity.

1.2. Data Acquisition

[8] The Fanshawe section was surveyed using a Nikon Total Station to define a perimeter grid which divided the section into ten 4.50 m $\times$ 3.00 m subsections which were further divided to yield forty 2.25 m $\times$ 1.50 m quadrants. Each subsection and quadrant was photographed using 100 ASA color slide film and digitally scanned as 24 bit color images at a resolution of 2700 dots per inch. Digital images were converted to 8 bit gray scale and resized to common dimensions of 2700 $\times$ 1800 pixels with corresponding pixel resolutions of 1.7 mm for the subsection data set and 0.8 mm for the quadrant data set. Subsection images are aligned using surveyed fiducial markers pinned and painted on the section face; a mosaic of the subsection data set is shown as Figure 1.

2. Spectral Transform Texture Segmentation

[9] The S transform is an innovative space-local spectral transform first presented by *Stockwell et al.* [1996]. In two dimensions, S transform analysis allows for the examination of the local spatial frequency content of an image $I(x, z)$ at each coordinate pair. The method of spectral

localization is similar to a wavelet transform [*Kaiser*, 1994; *Hubbard*, 1998], but the S transform is distinguished by the fact that the window and basis functions are separated and while they both dilate, only the window function translates. In its basic form, the S transform is also akin to a Gabor transform for which the window length varies with frequency [*Zayed*, 1996]. The S transform finds application in cases where the dominant frequency of a signal changes with space or time. It has proven useful for analyzing the Wolf sunspot series [*Mansinha et al.*, 1997b] for determining arrival times for different phases in an earthquake signal [*Pinnegar and Mansinha*, 1999], and for frequency visualization in seismic cross sections [*Theophanis and Queen*, 2000]. Frequency, in effect, is a representation of the rate of tonal change for an image. Therefore the applicability of S transform analysis should extend to texture segmentation.

[10] *Mansinha et al.* [1997a] define the S transform of a continuous two-dimensional image $I(x', z')$ as

$$S(x,z,k_x,k_z) = \int_{-\infty}^{\infty}\int_{-\infty}^{\infty} I(x',z') \cdot \frac{|k_x||k_z|}{2\pi} \cdot \exp\left\{-\frac{(x'-x)^2k_x^2+(z'-z)^2k_z^2}{2}\right\} \cdot \exp\{-i2\pi(k_xx'+k_zz')\}dx'dz' \quad (1)$$

where x, z and x', z' are both spatial coordinate pairs and k_x, k_z are the components of the wave number (spatial frequency) vector in the horizontal and vertical directions respectively. Accordingly, S is a complex surface in four dimensions. In one dimension, the k_x voice of $S(x, k_x)$ can be interpreted as the portion of $I'(x')$ represented by the basis function of wave number k_x where $I'(x')$ is $I(x')$ modulated by a Gaussian envelope centered at x with a standard deviation of $1/k_x$. The interpretation can similarly be extended to two dimensions. Wave numbers are the inverse of wavelength and, thus the footprint area of the modulating Gaussian is proportional to the product of the wavelengths being analyzed.

[11] The two-dimensional S transform of I can also be cast in terms of its Fourier spectrum H, thereby allowing calculation algorithms to take advantage of existing fast Fourier transform (FFT) routines. If a two-dimensional image is discretized as $I[xD_x, zD_z]$ where $x = [0, 1, \ldots, N-1]$ and $z = [0, 1, \ldots, M-1]$ and D_x and D_z are the spatial sampling intervals in the horizontal and vertical directions respectively, then

$$S\left[xD_x, zD_z, \frac{n}{ND_x}, \frac{m}{ND_z}\right] = \sum_{n'=0}^{N-1}\sum_{m'=0}^{M-1} H\left[\frac{n'+n}{ND_x}, \frac{m'+m}{MD_z}\right] \cdot \exp\left\{-2\pi^2\left(\frac{n'^2}{n^2}+\frac{m'^2}{m^2}\right)\right\} \cdot \exp\left\{i2\pi\left(\frac{n'x}{N}+\frac{m'z}{M}\right)\right\} \quad (2)$$

for $n, m \neq 0$. In this formulation, the x, z pair represents the spatial plane and the n, m and n', m' pairs represent the wave number (spatial frequency) plane. The algorithm for the computation of the n, m voice of S for all x, z is based on the method presented by *Eramian et al.* [1999]:

1. Choose a particular n, m.
2. Using the FFT, compute $H[n'/ND_x, m'/MD_z]$, the Fourier transform of I.
3. Perform a wraparound shift of H by n, m intervals, i.e. $H[(n'+n)/ND_x, (m'+m)/MD_z]$ such that the n, m frequency component is located at the origin.
4. Modulate the shifted Fourier transform $H[(n'+n)/ND_x, (m'+m)/MD_z]$ by the Gaussian $\exp\{-2\pi^2(n'^2/n^2 + m'^2/m^2)\}$. Note that the Gaussian is zero-mean and therefore must be wrapped around the $N-1, M-1$ coordinate such that the Gaussian envelope is symmetric about the n, m frequency component.
5. Using the IFFT, compute the inverse Fourier transform of the product in step 4.

[12] Calculation of the entire S spectrum involves repeating steps 1 through 5 for all possible combinations of n, m. Being a complex function in four dimensions, S has the double precision storage requirement of $2 \times N^2 \times M^2 \times 8$ bytes. For the Fanshawe section images, calculation of S results in a storage requirement of approximately 400 terabytes per subsection image. To make calculation of the S spectrum computationally tractable, additional simplifications are imposed: (1) Only the magnitude or the power of the complex S transform is retained in calculations. Henceforth the notation $S(x, z, k_x, k_z)$ reflects this simplification. (2) Calculation of the S transform is band-limited in wave number space. (3) Calculation of the S transform is executed in an overlapped block-processing scheme.

[13] In many cases, there will be a small range of important wave numbers that contribute most of the power to the S spectrum. Furthermore, when band-limiting the S spectrum, it is important to realize that significant power may exist for negative wave vectors. When analyzing images without appreciable directional asymmetry (such as an arrangement of close-packed circles), calculation requirements for the S transform can be further reduced by considering only fully positive wave numbers.

2.1. Spectral Manifestation of Texture

[14] Figure 2a shows the magnitude of the local S spectrum $S_{xz}(k_x, k_z)$ for the Fanshawe section coordinates x = 8.45 m, z = 2.35 m. The spectrum was calculated for horizontal and vertical wavelengths between 2 mm and 86 mm using an approximately 90 mm × 90 mm portion of the high-resolution, quadrant data set. Power can be seen to be distributed throughout most of the spectrum with appreciable content below wave numbers of 300 m^{-1} corresponding to a wavelength of 3.3 mm. In comparison, Figure 2b shows the magnitude of the local S spectrum calculated for the coarse grain region centered at the approximate Fanshawe section coordinates x = 6.95 m, z = 1.00 m. The coarser nature of this region manifests itself in the shift of power toward lower wave numbers or longer wavelengths. Quantification of these changes in local spectral power allows for analysis of image texture.

2.2. Texture Segmentation

[15] The local frequency content of an image, as provided by the S transform, contains information regarding the texture of an image. However, visualization of a four-

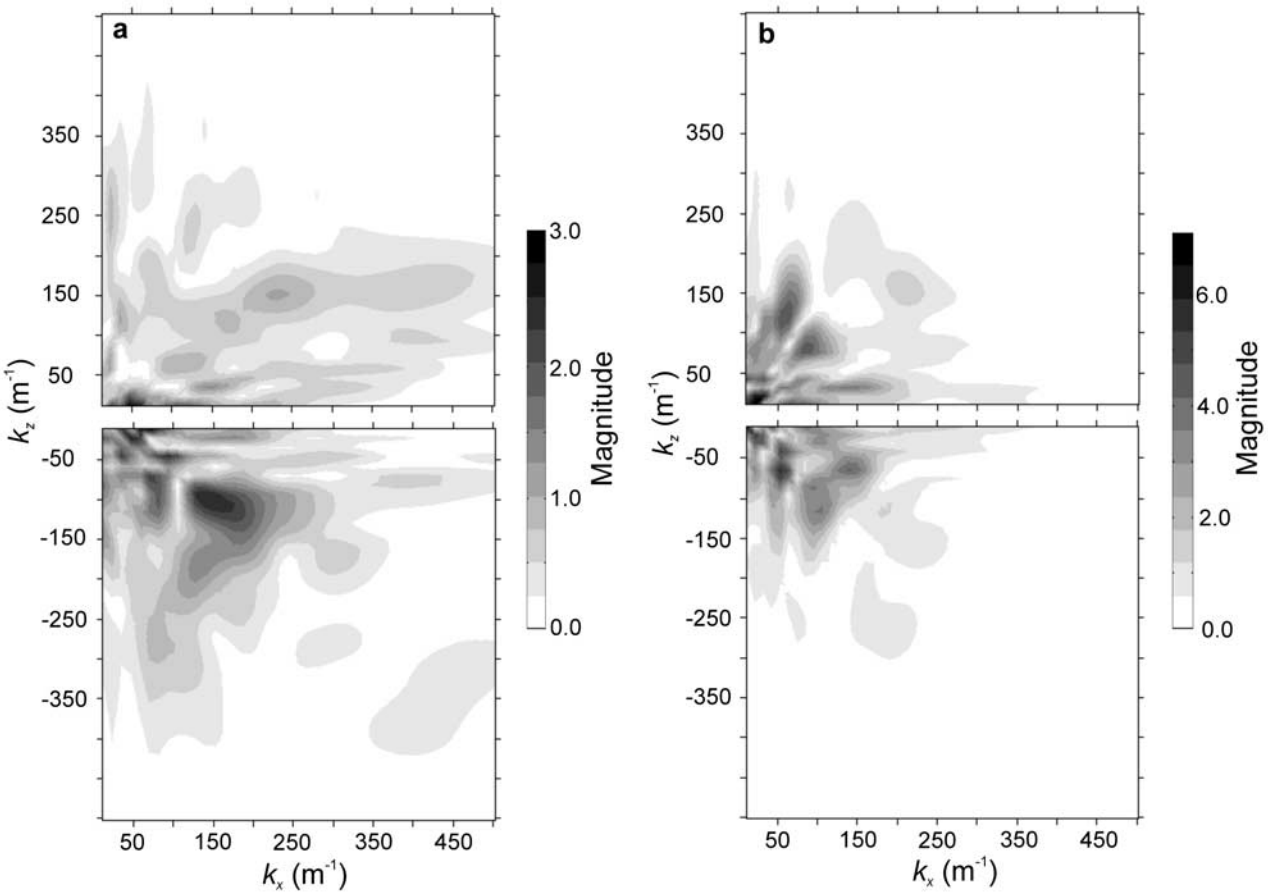

Figure 2. Local S spectrum magnitude $S_{xz}(k_x, k_z)$. (a) Fine-grained S spectrum at the coordinates $x = 8.45$ m, $z = 2.35$ m. (b) Coarse-grained S spectrum at the coordinates $x = 6.95$ m, $z = 1.00$ m.

dimensional (complex) surface and extraction of a meaningful measure of texture are not trivial. Based on the hypothesis that changes in the local spectrum reflect changes in texture, several texture segmentation methods can be developed based on collapsing each local S spectrum to a scalar measure of texture. Techniques include dominant wave number mapping [*Mansinha et al.*, 1997b], binary encoding and angular differencing [*Eramian et al.*, 1999]; the strengths and weaknesses of each are discussed in detail by *Oldenborger* [2000]. In response to this evaluation, the wave number-weighted scalar product was developed to optimize performance, robustness, simplicity and computational expediency when collapsing the S transform.

2.3. Wave Number-Weighted Scalar Product

[16] At each coordinate pair, the wave number-weighted scalar product (WSP) collapses the local spectrum magnitude $S_{xz}(k_x, k_z)$ to a scalar measure of texture T_{xz} according to the normalized scalar product

$$T_{xz} = \frac{S_{xz} \cdot W}{|S_{xz}||W|} \tag{3}$$

where W is a weight matrix, $S_{xz} \cdot W$ is the sum of the element-wise products, and $|S_{xz}|$ and $|W|$ represent the matrix magnitudes as the square roots of the sums of the squares of the elements. To capture the distribution of power in each local spectrum, the weight matrix is defined as $W = k_{xz}$ where k_{xz} is the matrix of wave vector magnitudes corresponding to the components of S_{xz}; energy present in the local spectrum is weighted linearly by the spatial frequency at which it occurs. Accordingly, power present in the local spectrum at high wave numbers, or short wavelengths, will be heavy-weighted; hence, high values of T will correspond to fine textures. Conversely, power present in the local spectrum at low wave numbers, or long wavelengths, will be light-weighted and low values of T will correspond to coarse textures.

[17] WSP segmentation suffers from the same nonuniqueness as the familiar scalar product of vectors: many different vector pairs may yield the same scalar product. Specifically, WSP segmentation may not discriminate between high power at low wave numbers or low power at high wave numbers. Unfortunately, when collapsing a four-dimensional function to two dimensions, loss of information is inevitable. However, we can rationalize that if power is not too diffuse, variations in spectral content will be adequately captured by WSP segmentation.

3. Fanshawe Section Texture Maps

[18] Through examination of the local spectra for typical fine-, medium- and coarse-grain regions across the Fanshawe section, it was determined that the majority of

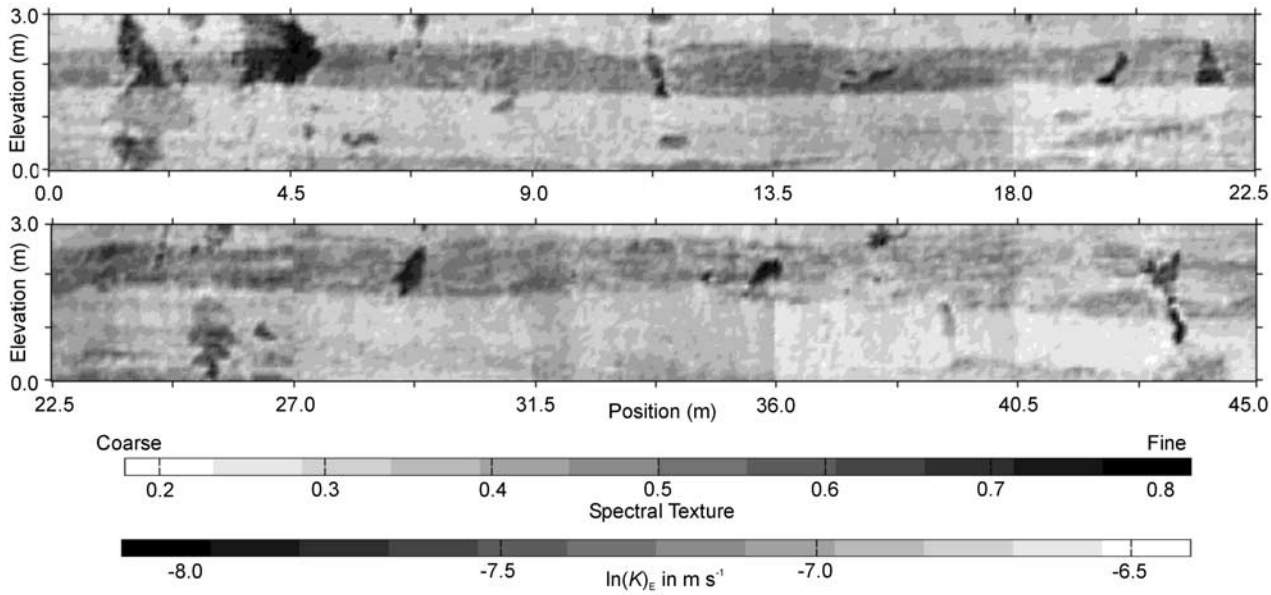

Figure 3. Spectral texture map and estimated log-transformed hydraulic conductivity field for the Fanshawe section.

spectral information is located between wavelengths of approximately 3 mm to 45 mm with mean dominant wave vector magnitudes ranging from about 125 m^{-1} to 35 m^{-1} (corresponding to wavelengths of 8 mm and 29 mm respectively).

[19] Since image texture, like hydraulic conductivity, is scale-dependent [*Drury*, 1993], it is likely that different bandwidths will dominate the S spectrum at the microscale and at the outcrop scale. Analysis of synthetic images indicates spectral power concentration at wavelengths equal to the grain dimension, twice the grain dimension and twice the grain spacing [*Oldenborger*, 2000]. While length scales associated with grain spacing are below the limiting Nyquist wavelength and may even be too small to be photographically imaged, length scales of 3 mm to 45 mm correspond well to dimensions expected for (twice) the mean resolvable grain diameters of the Fanshawe section.

[20] However, looking at Figure 2, it can be seen that local spectra do exhibit some energy at wave numbers below 35 m^{-1}. Some of this energy is attributed to the inherent periodicity of a discrete image-processing block at wavelengths equal to the block dimensions and it is important not to attribute this energy to textural properties. To reduce these energy contributions, image processing block dimensions are required to be at least twice the maximum analyzed wavelength.

[21] Texture was calculated at each pixel of the ten subsection images of the Fanshawe section (Figure 1) using the WSP texture segmentation algorithm for fully positive wave numbers between the wavelength limits of 3.5 mm to 45 mm. Results are presented as Figure 3. For the given analysis bandwidth, memory constraints limit processing block size to approximately 130 mm $\times$ 130 mm. Reducing processing block size reduces memory requirements and decreases computation time but results in narrower possible bandwidths and noisier image segmentation. To maintain continuity of results in a block-processing scheme, image-processing blocks are overlapped by 20% on every side within a subsection image; only the nonoverlapping portions of the texture map are retained. Edge effects can still be observed at the seams between subsection images due to the lack of overlap.

[22] While edge effects and small errors in survey contiguity explain discontinuities present at the seams between the subsection images, they cannot explain the large-scale differences observed between entire subsections. Specifically, texture values for subsections 4 (x = 13.5–18.0 m), 6 (x = 22.5–27.0 m) and 8 (x = 31.5–36.0 m) are slightly higher than those for the rest of the section and texture values for subsections 5 (x = 18.0–22.5 m), 9 (x = 36.0–40.5) and 10 (x = 40.5–45.0 m) appear slightly lower than those for the rest of the section. The analysis bandwidth and thus the weight matrix W are constant across the entire Fanshawe section, and therefore equivalent local spectra map to equivalent values of T across subsection images. Furthermore, in accordance with the normalized formulation of the WSP, differences in spectral magnitude should not affect texture segmentation; a spectrum with high amplitude is collapsed via the WSP to the same texture value as a spectrum with low amplitude, providing that the relative frequency contents are equal. However, variations in photographic conditions (lighting and exposure) and the nonlinear properties of film development and digital scanning may not preserve the relative frequency content between images. The result is nonuniformity of image intensity [*Schincariol et al.*, 1993] which leads to discontinuities of spectral texture across subsection boundaries. For example, overexposure and underexposure, or more generally, reductions in photographic contrast, act to remove high frequency variations in tone [*Drury*, 1993]. In the case of overexposure, the low-pass filtering phenomenon may be familiarly referred to as washing out and is obviously visible for several portions of the Fanshawe section data set (Figure 1).

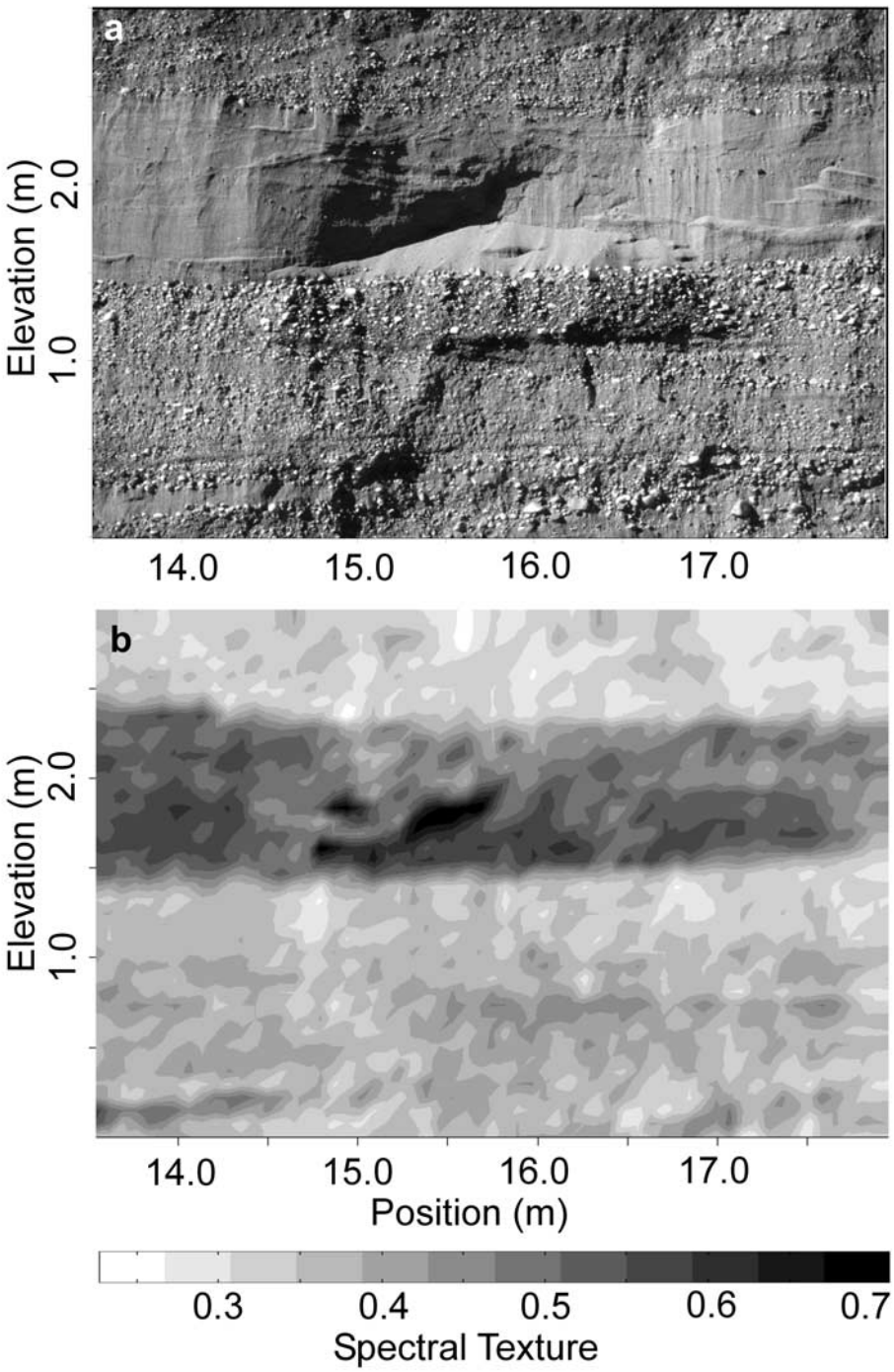

Figure 4. (a) Subsection 4 of the Fanshawe section. (b) Spectral texture map for subsection 4 of the Fanshawe section.

[23] Visually, the WSP texture map is representative of the sedimentary structures present in the Fanshawe section. Subsection 4 provides a good example of the discrimination ability of WSP texture segmentation (Figure 4). In addition to the obvious segmentation of the main sedimentary units, the sand lens located at approximately $x = 14$ m, $z = 0.25$ m is clearly imaged as a fine texture within the coarse textured lower gravel unit. The coarse cobbles along the bottom of the subsection, as well as the coarse cobbles just below the middle sand unit, are represented by the lower limit of T. The inclined structures of repeating sand and gravel within the top 0.5 m of the subsection are not as clearly imaged, but some inclined texture is visible. The inclined features have a mixed positive/negative wave number component and thus are only partially detected by an analysis using only fully positive wave numbers.

[24] As can be seen from the texture maps of most of the subsections, the WSP texture segmentation algorithm

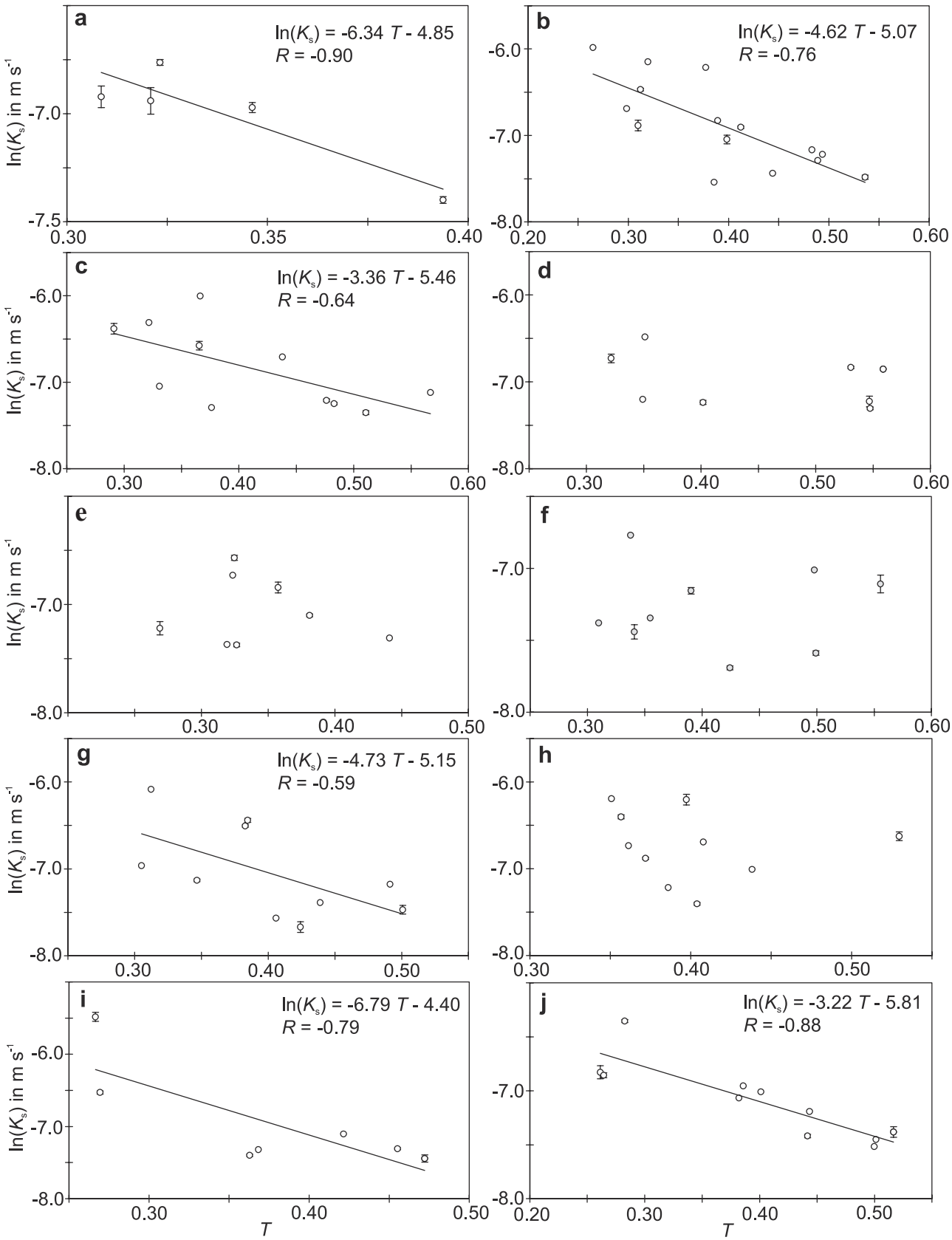

Figure 5. (a–j) Observed correlation between collocated measurements of hydraulic conductivity $\ln(K_s)$ and WSP texture T for subsections 1 through 10 of the Fanshawe section. Linear regression is presented only for those subsections for which the correlation coefficient exceeds the critical value at the 95% significance level. Vertical bars indicate the measurement error associated with hydraulic conductivity.

is sensitive to shadows. Because the texture segmentation routine involves a local Gaussian window, it is able to work around shadows that are small with respect to wavelength. However, for extensive shadows, the local spectra may be noisy and/or low-power resulting in the mapping of shadow cores with erroneously high texture values.

3.1. Correlation With Hydraulic Properties

[25] Undisturbed sediment cores (0.073 m diameter) were obtained across the Fanshawe section according to a stratified random sampling scheme [*Gilbert*, 1987; *Oldenborger et al.*, 2002]. Constant-head permeameter measurements [*Oldenborger*, 2000] for these cores allow for quantitative comparison of WSP texture with log-transformed hydraulic conductivity. Figure 5 illustrates the observed relationships between collocated spectral texture T and log-transformed hydraulic conductivity $\ln(K_s)$ on a subsection basis. Plotted T values were extracted from the high-resolution texture maps using a low-pass decimation filter in order to generate values of spectral texture representative of a region equal in area to the sediment cores (70 mm pixel resolution). On a sample-by-sample basis, texture values were deemed as reliable or unreliable based on their location in shadow zones, in overexposed regions, on slump features, or on sedimentary interfaces. Out of 122 possible sample locations, 94 are employed for Figure 5 and further analysis.

[26] Meaningful correlation exists between T and $\ln(K_s)$ for over half of the subsections. For subsections 1, 2, 3, 7, 9 and 10, the degree of correlation, as measured by the correlation coefficient R, is statistically significant [*McBean and Rovers*, 1998] and a linear regression is warranted. Discrepancies in the calculated gradients between these subsections are due, in part, to unavoidable variation of the least squares fit between subsections. More importantly, these discrepancies are a result of the nonuniformity of image intensity between subsections.

[27] Subsections 4, 5, 6 and 8 simply do not show a statistically significant correlation between WSP-derived texture and $\ln(K_s)$. In these cases, it may be that the subsection data are not sufficient to define a recognizable trend; local spectra of the photographic images may not be representative of the physical surface textures at enough sediment core locations. We speculate that the natural lighting may be a contributing factor. The surface of the Fanshawe section is not entirely planar. Deviations of the surface from planar cause abrupt local changes in the lighting angle that result, not only in large portions of solid shadow but, also, in localized regions of spotty shadow which may be erroneously interpreted as sedimentary texture. Areas of spotty shadow are most obvious for subsection 6 between 24 m and 25 m and for subsection 8 between 32 m and 34 m (Figure 1).

[28] A further contribution to degradation of any K-T correlation may be the dependency of hydraulic conductivity on grain size distribution. Aeolian erosion removes significant amounts of the fine sand matrix from the cliff face on very short timescales. What is left on the surface to be imaged is the coarser gravel. It is often the fine particles combined with packing arrangement that dominate the hydraulic conductivity of the media [*Koltermann and Gorelick*, 1995], and thus under some conditions, physical surface textures may not be entirely representative of hydraulic conductivity.

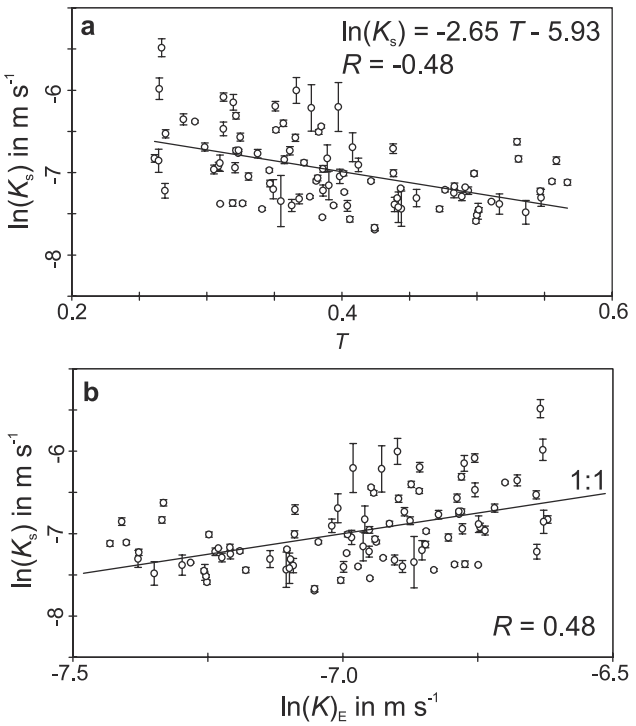

Figure 6. (a) Observed correlation between collocated measurements of hydraulic conductivity $\ln(K_s)$ and WSP texture T. (b) Measured versus estimated hydraulic conductivity. Vertical bars indicate the measurement error associated with hydraulic conductivity.

[29] However, these sources of error should apply equally to all image subsections. If the subsection texture maps are regarded as subsets of a total data set, it is not unreasonable that certain subsets may not exhibit the global trend. Although the individual subsections show greater degrees of correlation between T and $\ln(K_s)$, and variations in photographic properties may contribute to subsection-specific K-T relationships, an estimate of the hydraulic conductivity field for the entire section is the ultimate goal. To this end, the degree of correlation can be examined for the combined, full-section data (Figure 6a). Correlation is statistically significant and can be described by the linear relationship

$$\ln(K)_E = -2.65T - 5.93 \quad (4)$$

which when applied to the texture map, yields the estimated log-transformed hydraulic conductivity field (Figure 3). Reproduction of all of hydraulic conductivity measurements by the estimated hydraulic conductivity field is only as good as the K-T relationship (Figure 6b).

3.2. Spatial Statistics

[30] Using simple semivariogram analysis [*Isaaks and Srivastava*, 1989; *Deutsch and Journel*, 1992], the spatial statistical structure of spectral texture can be compared to

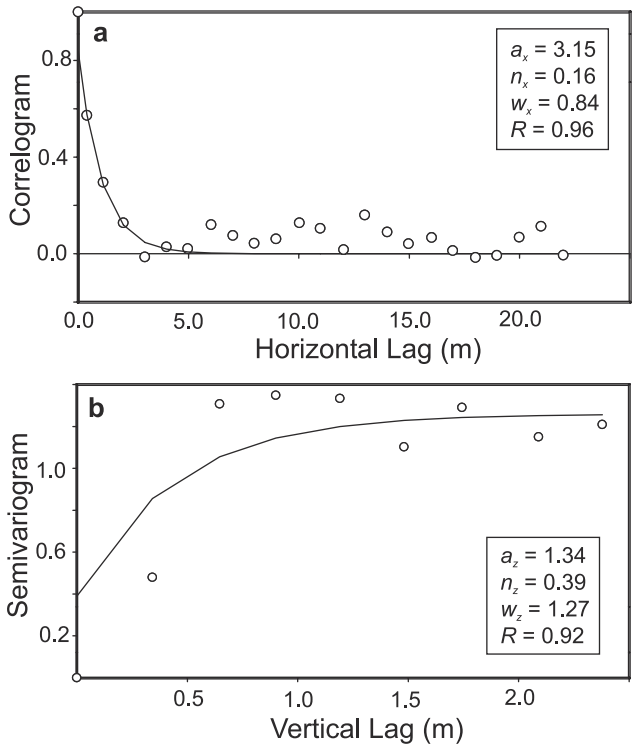

Figure 7. Experimental and model geostatistics for log-transformed hydraulic conductivity. (a) Horizontal correlogram. (b) Vertical semivariogram. Points indicate calculated geostatistical values based on core permeameter measurements; solid lines indicate the optimum least squares solutions corresponding to the listed model parameters.

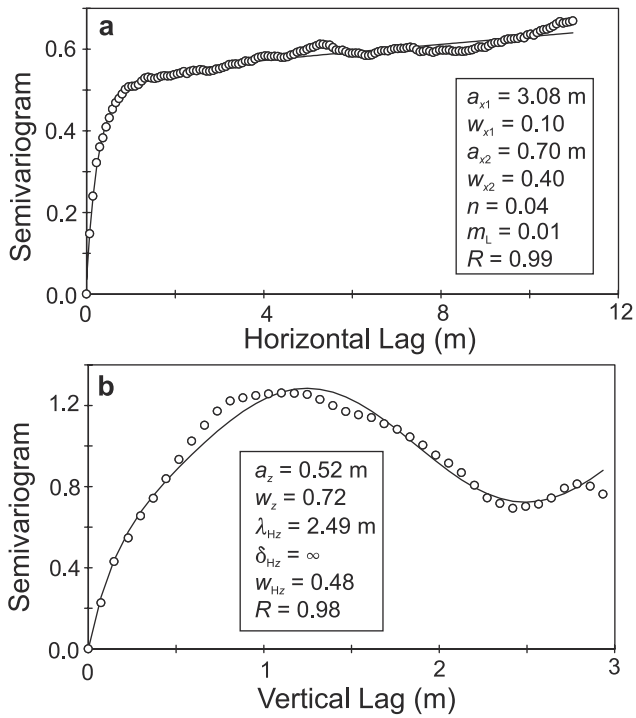

Figure 8. Experimental and model geostatistics for the spectral texture map of the Fanshawe section. (a) Horizontal semivariogram. (b) Vertical semivariogram. Points indicate calculated geostatistical values based on WSP texture; solid lines indicate the optimum least squares solutions corresponding to the listed model parameters.

that of the sample hydraulic conductivities. Figure 7 shows the horizontal correlogram and the vertical semivariogram calculated for $\ln(K_s)$. Both curves are best fit with simple exponential models with parameters summarized in Table 1. Figure 8 shows the horizontal and vertical semivariograms calculated for the decimated full-section spectral texture map. Horizontal texture data are best fit with a nested exponential model of the form

$$\gamma(h) = n + \sum_{i=1}^{2} w_i\left(1 - e^{-3h/a_i}\right) + m_L h \qquad (5)$$

where γ is the semivariogram statistic, h is the lag, n is the nugget, a is the range, w is the weight and m_L is the linear drift. Results are summarized in Table 1. For the texture data, the secondary horizontal range of 3.08 m is very similar to the horizontal range of 3.15 m determined for $\ln(K_s)$. However, because of the sensitivity of the texture maps to (spotty) shadows and photographic discontinuities, significant amounts of uncorrelated, nontextural information or noise can be expected for the texture maps; these features are manifest in the sub-meter primary range of 0.70 m. Additional nonstationary contributions from lighting variations, including large shadow zones, may contribute to the minor linear drift observed for the horizontal semivariogram of texture. *Rea and Knight* [1998] note that visual estimates of correlation length will consistently exceed those obtained from variogram analysis; the semivariogram is an estimator of linear continuity whereas the human eye tends to trace nonlinear, continuous features. This difference is apparent when looking at the Fanshawe section (Figure 1). Visually, the section appears more continuous than indicated by the calculated horizontal ranges.

[31] In the vertical direction, the semivariogram of spectral texture is best fit with nested exponential and hole-effect models where the hole-effect is characterized by a hole wavelength λ_H, a damping factor δ_H, and a weight w_H [*Journel and Froidevaux*, 1982]. The nested exponential range of 0.51 m may be representative of within-facies heterogeneity whereas the observed vertical hole wavelength of 2.49 m (Table 1) represents the period of oscillation from coarse to fine back to coarse texture. No such oscillation was observed for the $\ln(K_s)$ data set possibly due to sparsity of data pairs in the vertical direction. The vertical

Table 1. Comparison of the Spatial Statistics of Texture T and Log-Transformed Hydraulic Conductivity $\ln(K_s)$

	Horizontal					
	a_{x1}, m	w_{x1}	a_{x2}, m	w_{x2}	n_x	m_{Lx}, m^{-1}
$\ln(K_s)$	3.15	0.84	NA	0.00	0.16	0.00
T	0.70	0.40	3.08	0.10	0.04	0.01
	Vertical					
	a_z, m	w_z	n_z	λ_{Hz}, m	δ_{Hz}, m	w_{Hz}
$\ln(K_s)$	1.34	0.87	0.39	NA	NA	0.00
T	0.52	0.72	0.00	2.49	∞	0.48

range of 1.34 m determined for $\ln(K_s)$ is comparable to that of a simple exponential model applied to the texture data.

4. Conclusions

[32] Presently, the advancement of the practice of predicting groundwater flow and the fate of contaminant transport is limited to a large extent by the need for accurate, macroscale knowledge of subsurface heterogeneity of porous media. Visually, WSP texture maps show excellent identification and discrimination of sedimentary textures. Geostatistical analyses of the texture maps suggest that the correlation structure of texture has a component similar to the correlation structure of the log-transformed hydraulic conductivity field. Furthermore, local linear relationships are observed between WSP texture and $\ln(K_s)$ which allow direct estimation of the hydraulic conductivity over subsection images and, with less confidence, over the entire Fanshawe section. Often, image textures may not be accurate representations of the surface textures due to variations in lighting. In some cases, the physical surface texture is simply not representative of the sedimentary material and a relationship between image texture and hydraulic conductivity cannot be expected. Additionally, when attempting to merge texture analysis of multiple images, nonuniformity of image exposure and contrast may result in a nonuniformity of the perceived frequency content between images despite a common frequency signature of the sedimentary material.

[33] As for many remote-sensing techniques, the relation of the proxy-measured property to the desired physical property presents a significant hurdle. For spectral texture analysis, the practitioner is able to assess the changes in the frequency content of photographic images of the media. However, the links between hydraulic conductivity, material texture, and image texture are neither linear nor stationary. To improve the robustness of S transform texture segmentation, several issues need to be addressed. It may be beneficial to collapse the four-dimensional S transform to an n-component vector measure of texture in order to increase discrimination of local spectra and possibly to include some indication of textural direction. To improve applicability of texture mapping over large regions covered by several photographic images of varying resolution, it may be necessary to pursue the ideal of equalized images not only in terms of pixel resolution but also in terms of a calibration of image intensity with some standard such as photographic optical density. Calibration may remove some degree of the process-induced nonuniformity between images that results in discontinuity of spectral texture. Similarly, more attention could be payed to acquiring images with continuous flat lighting and minimal shadow. Alternatively, as acquiring images without shadow is often impractical or impossible, attempts could be made to remove large regions of shadow before texture segmentation. However, the pretexture segmentation image processing options are unlimited and each step may take image properties further from representing the natural properties of the physical material.

[34] **Acknowledgments.** This research was funded by the Natural Sciences and Engineering Research Council of Canada through grants awarded to RAS and LM and through scholarships awarded to GAO. Lafarge Canada Inc. kindly provided access to their London gravel pits and the loan of heavy machinery. The authors would like to thank J. D. McNeil for assistance with field data acquisition and anonymous reviewers for helpful comments and criticisms.

References

Anderson, M. P., Hydrogeological facies models to delineate large-scale spatial trends in glacial and glaciofluvial sediments, *Geol. Soc. Am. Bull.*, *101*, 501–511, 1989.

Barnett, P. J., W. R. Cowan, and A. P. Henry, Quaternary geology of southern Ontario, southern sheet, *Ontario Geol. Surv. Map*, *2556*, scale 1:1000000, 1991.

Cassiani, G., and M. A. Medina Jr., Incorporating auxiliary geophysical data into ground-water flow parameter estimation, *Ground Water*, *35*(1), 79–91, 1997.

Deutsch, C. V., and A. G. Journel, *GSLIB, Geostatistical Software Library and User's Guide*, Oxford Univ. Press, New York, 1992.

Dreimanis, A., C. G. Winder, and R. A. Aaltonen, London, Ontario: Geology, geomorphology, geodata, in *Urban Geology of Canadian Cities*, edited by P. F. Karrow and O. L. White, pp. 237–260, Geol. Assoc. of Can., St. John's, Newfoundland, 1998.

Drury, S. A., *Image Interpretation in Geology*, 2nd ed., Chapman and Hall, New York, 1993.

Eramian, M. G., R. A. Schincariol, L. Mansinha, and R. G. Stockwell, Generation of aquifer heterogeneity maps using two-dimensional spectral texture segmentation techniques, *Math. Geol.*, *31*(3), 327–348, 1999.

Frind, E. O., E. A. Sudicky, and S. L. Schellenberg, Micro-scale modeling in the study of plume evolution in heterogeneous media, *Stochastic Hydrol. Hydraul.*, *1*, 263–279, 1987.

Gelhar, L. W., and C. L. Axness, Three-dimensional stochastic analysis of macrodispersion in aquifers, *Water Resour. Res.*, *19*(1), 161–180, 1983.

Gilbert, R. O., *Statistical Methods for Environmental Pollution Monitoring*, Van Nostrand Reinhold, New York, 1987.

Gillham, R. W., and J. A. Cherry, Contaminant migration in saturated unconsolidated geologic deposits, *Spec. Pap. Geol. Soc. Am.*, *189*, 31–62, 1982.

Hess, K. M., S. H. Wolf, and M. A. Celia, Large-scale natural gradient tracer test in sand and gravel, Cape Cod, Massachusetts, 3, Hydraulic conductivity variability and calculated macrodispersivities, *Water Resour. Res.*, *28*(8), 2011–2027, 1992.

Hubbard, B. B., *The World According to Wavelets*, 2nd ed., A. K Peters, Wellesley, Mass., 1998.

Hubbard, S. S., Y. Rubin, and E. Majer, Spatial correlation structure estimation using geophysical and hydrogeological data, *Water Resour. Res.*, *35*(6), 1809–1825, 1999.

Hyndman, D. W., and S. M. Gorelick, Estimating lithologic and transport properties in three dimensions using seismic and tracer data, the Kesterson aquifer, *Water Resour. Res.*, *32*(9), 2659–2670, 1996.

Isaaks, E. H., and R. M. Srivastava, *An Introduction to Applied Geostatistics*, Oxford Univ. Press, New York, 1989.

Journel, A. G., and R. Froidevaux, Anisotropic hole-effect modeling, *Math. Geol.*, *14*(3), 217–239, 1982.

Jussel, P., F. Stauffer, and T. Dracos, Transport modeling in heterogeneous aquifers, 1, Statistical distribution and numerical generation of gravel deposits, *Water. Resour. Res.*, *30*(6), 1803–1817, 1994.

Kaiser, G., *A Friendly Guide to Wavelets*, Birkhäuser, Boston, 1994.

Koltermann, C. E., and S. M. Gorelick, Fractional packing model for hydraulic conductivity derived from sediment mixtures, *Water Resour. Res.*, *31*(12), 3283–3297, 1995.

Koltermann, C. E., and S. M. Gorelick, Heterogeneity in sedimentary deposits, a review of structure-imitating, process-imitating and descriptive approaches, *Water Resour. Res.*, *32*(9), 2617–2658, 1996.

Mansinha, L., R. G. Stockwell, and R. P. Lowe, Pattern analysis with two-dimensional spectral localisation, applications of two-dimensional S transforms, *Physica A*, *239*, 286–295, 1997a.

Mansinha, L., R. G. Stockwell, R. P. Lowe, M. Eramian, and R. A. Schincariol, Local S-spectrum analysis of 1-D and 2-D data, *Phys. Earth Planet. Inter.*, *103*, 329–336, 1997b.

Mavko, G., T. Mukerji, and J. Dvorkin, *The Rock Physics Handbook, Tools for Seismic Analysis in Porous Media*, Cambridge Univ. Press, New York, 1998.

McBean, A. E., and F. A. Rovers, *Statistical Procedures for Analysis of Environmental Monitoring Data and Risk Assessment*, Prentice Hall, Old Tappan, N. J., 1998.

Oldenborger, G. A., Characterizing the spatial distribution of hydraulic conductivity, application of ground-penetrating radar and space-local

spectral techniques, M.Sc. thesis, Univ. of West. Ontario, London, Ontario, Canada, 2000.

Oldenborger, G. A., R. A. Schincariol, and L. Mansinha, Radar determination of the spatial structure of hydraulic conductivity, *Ground Water*, in press, 2002.

Pal, N. R., and S. K. Pal, A review on image segmentation techniques, *Pattern Recognition*, *26*(9), 1277–1294, 1993.

Pinnegar, C. R., and L. Mansinha, Causal forms of the S-transform, *Eos Trans. AGU*, *80*(17), Spring Meet. Suppl., S218, 1999.

Poeter, E., and D. R. Gaylord, Influence of aquifer heterogeneity on contaminant transport at the Hanford site, *Ground Water*, *28*, 900–909, 1990.

Rea, J., and R. Knight, Geostatistical analysis of ground-penetrating radar data: A means of describing spatial variation in the subsurface, *Water Resour. Res.*, *34*(3), 329–339, 1998.

Schincariol, R. A., E. E. Herderick, and F. W. Schwartz, On the application of image analysis to determine concentration distributions in laboratory experiments, *J. Contam. Hydrol.*, *12*, 197–215, 1993.

Schincariol, R. A., F. W. Schwartz, and C. A. Mendoza, Instabilities in variable density flows: Stability and sensitivity analysis for homogeneous and heterogeneous media, *Water Resour. Res.*, *33*(1), 31–41, 1997.

Stockwell, R. G., L. Mansinha, and R. P. Lowe, Localization of the complex spectrum: The S transform, *IEEE Trans. Signal Processes*, *44*(4), 998–1001, 1996.

Sudicky, E. A., J. A. Cherry, and E. O. Frind, Migration of contaminants in groundwater at a landfill: A case study, *J. Hydrol.*, *63*, 81–108, 1983.

Theophanis, S., and J. Queen, Color display of the localized spectrum, *Geophysics*, *65*(4), 1330–1340, 2000.

Yeh, T.-C., J. Mas-Pla, T. M. Williams, and J. F. McCarthy, Observation and three-dimensional simulation of chloride plumes in a sandy aquifer under forced-gradient conditions, *Water Resour. Res.*, *31*(9), 2141–2157, 1995.

Zayed, A. I., *Handbook of Function and Generalized Function Transformations*, CRC Press, Boca Raton, Fla., 1996.

L. Mansinha and R. A. Schincariol, Department of Earth Sciences, University of Western Ontario, London, Ontario, Canada, N6A 5B7.

G. A. Oldenborger, Center for Geophysical Investigation of the Shallow Subsurface, Boise State University, Boise, ID, 83725, USA. (greg@cgiss.boisestate.edu)